

# The Transient Dynamics of the Turbulent Central Molecular Zone

Jesus M. Salas,<sup>1\*</sup> Mark R. Morris<sup>1</sup> and Smadar Naoz<sup>1,2</sup>

<sup>1</sup>*Dept. of Physics & Astronomy, University of California, Los Angeles, CA, 90095, USA*

<sup>2</sup>*Mani L. Bhaumik Institute for Theoretical Physics, Department of Physics and Astronomy, University of California, Los Angeles, CA 90095, USA*

21 April 2022

## ABSTRACT

The Central Molecular Zone, which spans up to about 500 pc around the center of our Galaxy, consists of a turbulent and complex gaseous environment predominantly in the form of relatively dense molecular gas. Here we explore the effect of turbulence on the gas dynamics of this region. We use Smoothed Particle Hydrodynamics simulations, which include self-gravity and a recipe for turbulence driving, to follow the long-term evolution of the gas in the rotating bar potential of the Galaxy. We find that before the system reaches a steady state, a twisted ring is formed, similar to the observed one. As expected, this feature later dissipates leaving a smooth gaseous disk. We also find that the average densities resulting from our simulations are, in the absence of major perturbations, consistent with the observed ones. Our results suggest that the current gas in the Central Molecular Zone is not in a steady state.

## 1 INTRODUCTION

The main gaseous feature of the Galactic Center (GC) - the Central Molecular Zone (CMZ), has a rich and complex structure that extends over a galactocentric radius of  $\sim 500$  pc and contains a mass of  $M \sim 3 - 7 \times 10^7 M_{\odot}$  (Morris & Serabyn 1996). The observed physical properties of the interstellar medium in the CMZ are very different from those typically found in molecular clouds in the Galactic disc. It is largely composed of relatively dense ( $n \sim 10^3 - 10^5 \text{ cm}^{-3}$ ) and warm gas ( $\sim 70 - 100$  K on average, e.g., Güsten et al. 1981; Morris et al. 1983; Huettemeister et al. 1993; Ao et al. 2013), mostly condensed into Giant Molecular Clouds (GMCs) or dense tidal streams of molecular gas. The molecular gas in the CMZ also appears to have thermal, turbulent and magnetic pressures much higher than those present in the large-scale Galactic disk (Spergel & Blitz 1992).

The gas dynamics in the inner part of the Galaxy have been studied extensively in the literature using numerical simulations. For example, some studies have simulated the dynamics of gas in the CMZ under realistic gravitational potentials (e.g., Kim et al. 2011; Lucas 2015; Ridley et al. 2017; Shin et al. 2017; Sormani et al. 2018). In most of these studies, the gas initially settles into  $X_1$  orbits, which occur between the corotation radius and the inner Lindblad resonance (ILR) of the bar potential. As inwardly migrating gas approaches the ILR, there is an innermost stable  $X_1$  orbit inside of which the orbits become self-intersecting. The gas compresses and shocks near the edges of these orbits, loses angular momentum and descends onto  $X_2$  orbits, which are closed and elongated orbits that have their long axes oriented perpendicular to the bar (Binney et al. 1991; Athanassoula 1992; Jenkins & Binney 1994; Gerhard 1996).

The shocks along the innermost  $X_1$  orbit are presumed responsible for compressing the gas into molecular form, and the accumulated molecular gas on  $X_2$  orbits comprises the observed CMZ. However, it is unclear how fast molecular gas is transported further in toward the GC, and which mechanisms are responsible for its transport.

There have also been more general dynamical studies of gas in large-scale Galactic barred potentials (e.g., Sormani et al. 2015a,b; Portail et al. 2017). Most of these simulations do not include self-gravity, which is more computationally expensive and requires large thermal energies ( $T \sim 10^3 - 4$  K) or rotational support to prevent the gas from collapsing into dense clumps. While the addition of self-gravity in simulations of gas orbiting in galactic potentials is computationally expensive, some steps have been taken (examples of simulations that include self-gravity are Wada 2001; Namekata & Habe 2011; Khoperskov et al. 2013).

While self-gravity is a key factor in understanding the dynamics in the CMZ, turbulence in this medium seems to greatly influence the physical processes there. The relatively high gas temperatures (70–100 K) are one of the key properties of CMZ clouds, and there is evidence showing that the gas is kept warm by the dissipation of turbulence (Immer et al. 2016; Ginsburg et al. 2016). It has also been suggested that turbulence plays a role in the suppression of star formation (e.g., Kruijssen et al. 2014). However, the driving mechanism for the turbulence in CMZ clouds has not been conclusively identified (see Kruijssen et al. 2014 for a discussion about possible sources of turbulence). Furthermore, the large turbulent velocity dispersion in CMZ must be responsible for supporting the gas against gravitational collapse because the thermal pressure of the gas would be insuffi-

cient. This motivates the inclusion of turbulence to build a realistic model of self-gravitating gas dynamics in the CMZ.

Interstellar turbulence decays quite rapidly, on timescales of the order of the free-fall time of the system (e.g., [Mac Low 1999](#)). Therefore, energy must be injected into the system in order to maintain the turbulence. Simulations of turbulence-driven gas are generally employed in studies of the interstellar medium and star formation (e.g., [Stone et al. 1998](#); [Mac Low et al. 1998](#); [Krumholz & McKee 2005](#); [Burkhart et al. 2009](#); [Federrath et al. 2010](#)). However, there have been no studies of turbulence-driven gas in the CMZ to date. This is mainly due to the fact that performing a large-scale hydrodynamical simulation while simultaneously resolving turbulence on small scales would require extensive computational resources. In this paper, we avoid this problem by creating a simple model of turbulence driving, and applying it to a Smoothed Particle Hydrodynamics (SPH) code to study the large-scale dynamics of gas in the CMZ. Our main goal is to test the effectiveness of our turbulence algorithm to reproduce physical conditions, such as the density distribution and overall morphology, similar to those observed in the GC. This paper is organized as follows: Section 2 summarizes the numerical methods, which include a turbulence injection recipe. We present our main results in Section 3, and conclude in Section 4.

## 2 NUMERICAL METHODS

### 2.1 SPH code

We used the N-body/SPH code Gadget2 ([Springel 2005](#)), which is based on the tree-Particle Mesh method for computing gravitational forces and on the SPH method for solving the Euler equations of hydrodynamics. The smoothing length of each particle in the gas is fully adaptive down to a set minimum of 0.001 pc. Gadget2 employs an entropy formulation of SPH, as outlined in [Springel & Hernquist \(2002\)](#), with the smoothing lengths defined to ensure a fixed mass (i.e., fixed number of particles) within the smoothing kernel volume (set for  $N_{\text{neigh}} = 64$ ). The code adopts the Monaghan-Balsara form of artificial viscosity ([Monaghan & Gingold 1983](#); [Balsara 1995](#)), which is regulated by the parameter  $\alpha$ , set to 0.75.

We modified the standard version of Gadget2 to include turbulence driving, the gravitational potential of the Milky Way's inner 300 pc, and the effects of pressure by a surrounding medium. We describe these modifications below.

### 2.2 External Pressure

The interstellar medium of the GC is modeled via an external pressure term to approximate a constant pressure boundary. Following [Clark et al. \(2011\)](#), we modify Gadget2's momentum equation ([Springel & Hernquist 2002](#)):

$$\frac{d\mathbf{v}_i}{dt} = - \sum_{j=1}^N \left[ f_i \frac{P_i}{\rho_i^2} \nabla_i W_{ij}(h_i) + f_j \frac{P_j}{\rho_j^2} \nabla_j W_{ij}(h_j) \right] \quad (1)$$

where  $\mathbf{v}_i$  is the velocity of particle  $i$ ,  $P_i$  is the pressure,  $\rho_i$  is the density,  $W_{i,j}(h_i)$  is the kernel function which depends on the smoothing length  $h_i$ , and  $f$  is a unitless coefficient that depends on  $\rho_i$  and  $h_i$ . We replace  $P_i$  and  $P_j$  with  $P_i - P_{\text{ext}}$

and  $P_j - P_{\text{ext}}$ , respectively, where  $P_{\text{ext}}$  is the external pressure. The pair-wise nature of the force summation over the SPH neighbors ensures that  $P_{\text{ext}}$  cancels for particles that are surrounded by other particles. At the boundary, where the term does not disappear, it mimics the pressure contribution from a surrounding medium ([Clark et al. 2011](#)). We set  $P_{\text{ext}}$  equal to  $10^{10}$  ergs  $\text{cm}^{-3}$ , an approximate value for the GC ([Spergel & Blitz 1992](#); [Morris & Serabyn 1996](#)).

### 2.3 The galactic potential

We include into Gadget2 a bar-like gravitational potential of the inner region of the Galaxy, adopted from [Zhao et al. \(1994\)](#):

$$\Phi(r, \theta, \phi) = 4\pi G \rho_0 r_0^2 \left( \frac{r}{r_0} \right)^\alpha P(\theta, \phi), \quad (2)$$

where  $(r, \theta, \phi)$  are spherical coordinates fixed on the rotating bar, with the SMBH at  $r = 0$ , and  $P$  is the associated Legendre function,

$$P(\theta, \phi) = \frac{1}{\alpha(1+\alpha)} - \frac{Y(\theta, \phi)}{(2-\alpha)(3+\alpha)}. \quad (3)$$

$Y$  is a linear combination of spherical harmonic functions of the  $l = 2, m = 0, 2$  modes:

$$Y(\theta, \phi) = -b_{20}P_{20}(\cos \theta) + b_{22}P_{22}(\cos \theta) \cos 2\phi. \quad (4)$$

The parameter  $b_{20}$  determines the degree of oblateness/prolateness while  $b_{22}$  determines the degree of non-axisymmetry. Based on previous work by [Kim et al. \(2011\)](#), and most recently by [Gallego & Cuadra \(2017\)](#)<sup>1</sup>, we use the parameters:  $\alpha = 0.25$ ,  $b_{20} = 0.3$ ,  $b_{22} = 0.1$ ,  $\rho_0 = 40 \text{ M}_\odot \text{ pc}^{-3}$  and  $r_0 = 100$  pc. Given these parameters, a bar with axis ratio of [1: 0.74: 0.65] for the isodensity surface that intersects points  $[x = 0, y = \pm 200 \text{ pc}, z = 0]$  is obtained. In addition to the gravitational force due to the potential above, we introduced the rotation of the bar by adding centrifugal and Coriolis forces. We used the most recent estimate for the Galactic bar's pattern speed ( $\Omega_{\text{bar}} = 40 \text{ km s}^{-1} \text{ kpc}^{-1}$ ; [Bland-Hawthorn & Gerhard 2016](#); [Portail et al. 2017](#)).

### 2.4 Turbulence Driving

Driven turbulence is often modelled with a spatially static pattern for which the amplitude is adjusted in time following the methods introduced by [Stone et al. \(1998\)](#), [Mac Low et al. \(1998\)](#) and [Mac Low \(1999\)](#). Other studies use a forcing model that can vary in time and space (e.g., [Padoan et al. 2004](#); [Schmidt et al. 2006](#); [Federrath et al. 2010](#)). Both methods require Fourier Transforms on a cubic lattice with  $N^3$  points (or a square lattice with  $N^2$  on 2D simulations, where typical values for  $N = 128, 256, 1024$ , etc). By imposing this cubic lattice onto a simulation box with a physical size of  $L$  per side, we can use the separation between adjacent points ( $L/N$ ) as a proxy for the resolution of the turbulence. Hence, for a large-scale simulation of the CMZ, e.g.,  $L = 500$  pc, and simultaneously resolving turbulence on small scales,

<sup>1</sup> We note that there is a negative sign misprint in the potential equations shown in [Kim et al. \(2011\)](#) and [Gallego & Cuadra \(2017\)](#).

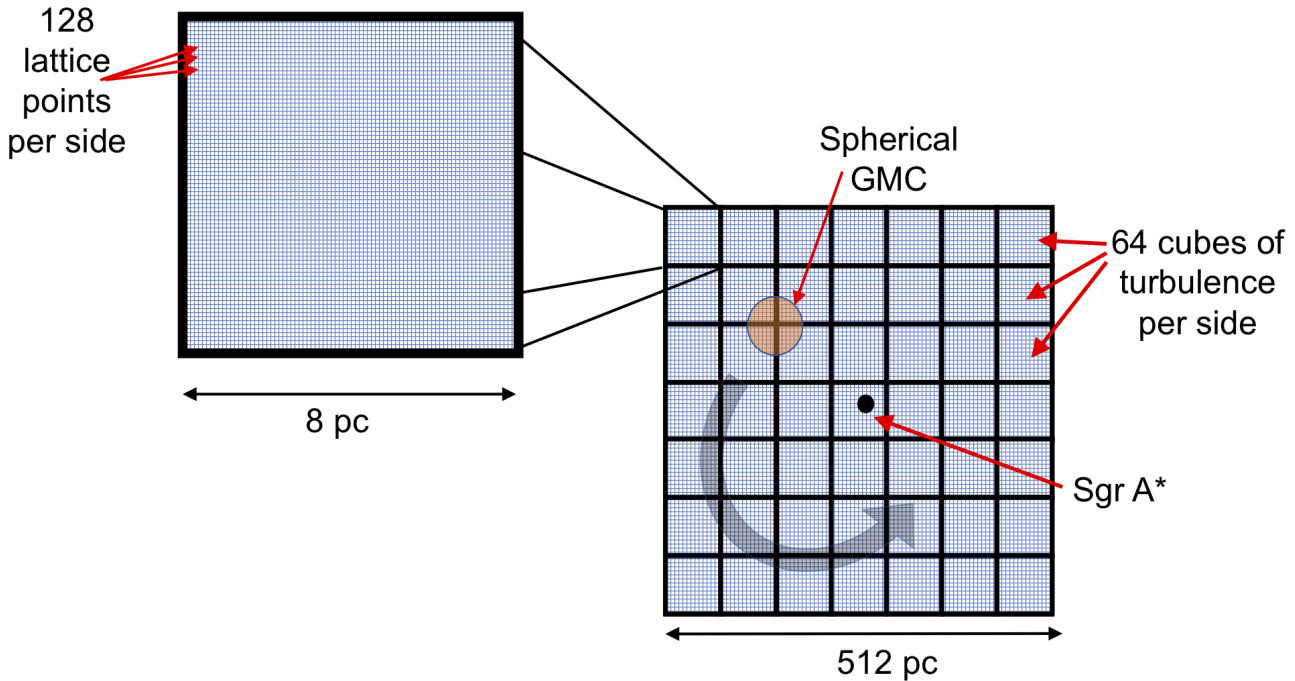


**Figure 1.** Two dimensional representation of our turbulence driving method. A single turbulence cube is shown on the left, while the combination of cubes to fill up the large simulation box is shown on the right. Note that the above schematic is intended for illustration purposes, since the number of cubes sketched is different from what we actually used.

e.g., 0.01 pc, the turbulence cube would have to contain  $N^3 = 5000^3$  points, which would require massive computational resources. To circumvent this problem, we instead use many smaller turbulence cubes to fill the volume of our larger simulation box, as follows:

First, we created a library of 10 files of turbulence, which our modified version of the Gadget2 code reads in at the start of the simulation. Each file contains a unique realization of a turbulent velocity field (in the form of a 3D matrix) with power spectrum  $P(k) \propto k^{-4}$  (suitable for compressible gas; e.g., Clark et al. 2011). Each of these 3D matrices of turbulence is generated using the method described in Rogallo (1981): via fast Fourier transforms inside a  $128^3$  box.

These 3D turbulence matrices can be visualized as lattice cubes with equally spaced lattice points, containing  $128 \times 128 \times 128$  points. We set the physical size of these cubes to be 8 pc per side, enough to fit an average GMC inside of it. Thus, the separation between two adjacent lattice points along one axis is  $8\text{pc}/128 = 0.0625$  pc.

In some studies, the driving module only contains power on the larger scales (e.g., Federrath et al. 2010). This type of driving models the kinetic energy input from large-scale turbulent fluctuations, which then break up into smaller structures as the kinetic energy cascades down to scales smaller than the turbulence injection scale. However, in SPH, the artificial viscosity may damp this energy cascade and prevent it from reaching the smaller scales. Consequently, to create the different realizations of turbulence velocity fields, we use a discrete range of  $k$  values from  $k_{min} = 2$  to  $k_{max} = 128$ , thus effectively injecting energy on scales between 4 pc ( $k = 2$ )

and 0.06 pc ( $k = 128$ ). To create the initial (turbulent) velocity field of an individual cloud (see Section 2.5), we use trilinear interpolation to calculate the velocity components for each SPH particle, based on that particle’s position on a turbulence cube. This interpolation method results in a turbulent velocity function  $\vec{I}(x, y, z)$ .

Next, we use  $64 \times 64 \times 64$  cubes of turbulence to fill up the volume of our large simulation box. This gives us a simulation box of size  $8\text{pc} \times 64 = 512$  pc per side. Using this method, the spatial resolution of the turbulence in our large simulation box is the same as the resolution of an individual turbulence cube. Each of the cubes that fill up the large simulation box is randomly chosen from our library of 10 files, thereby avoiding a velocity field that is coherent over scales greater than 8 pc. A representation of the method we describe here is shown in schematic form in Figure 1.

To drive the turbulence, we follow a method similar to that described by Mac Low (1999): every  $N_t$  timesteps (we fixed the timestep in all our simulations to  $\Delta t_s = 1000$  yrs) we add a velocity increment to every SPH particle, given by:

$$\Delta \vec{v}(x, y, z) = A \sqrt{G\rho} \vec{I}(x, y, z), \quad (5)$$

where  $\vec{I}(x, y, z)$  is the turbulent velocity interpolated from the turbulence field of the cube that contains the particle in question. The amplitude  $A$  is chosen to maintain a constant kinetic energy input rate  $E_{in} = \Delta E_{in}/(N_t \Delta t_s)$ , and the term  $\sqrt{G\rho}$  is added to counteract gravitational collapse by ensuring that higher-density regions receive more kinetic energy. Any particle outside the  $(512 \text{ pc})^3$  simulation box does not receive any turbulent energy. For compressible flow with a

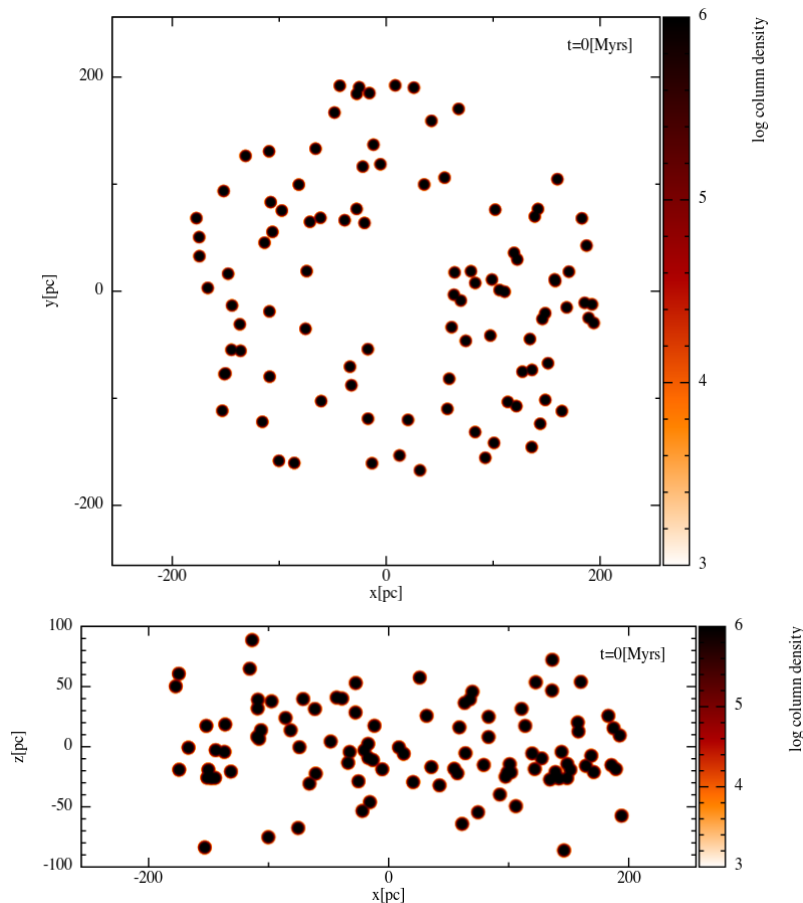


**Figure 2.** Top: x-y plane view of the initial state of the simulations. Color bar indicates column number density in log scale (units in  $\text{cm}^{-3} \text{ pc}$ ). Bottom: Edge-on view.

time-dependent density distribution, maintaining a constant kinetic energy input rate requires solving a quadratic equation in the amplitude  $A$  every time the driving is performed (Mac Low 1999). For  $N_{sph}$  particles of mass  $m_p$ , each with density  $\rho_i$ ,  $A$  is derived from (see Appendix A):

$$\Delta E_{in} = \frac{1}{2} m_p \sum_{i=1}^{N_{sph}} \left[ A^2 G \rho_i \vec{l}_i \cdot \vec{l}_i + 2A \sqrt{G \rho_i} \vec{l}_i \cdot \vec{v}_{l,i} \right]. \quad (6)$$

We take the larger root as the value for  $A$ . Finally, to mimic the random nature of turbulence, we change the turbulent velocity field of each of the  $64^3$  cubes every time the driving is performed. This is done by replacing each of the cubes with a different one, chosen randomly from the 10 files in our library. See Appendix A for further details.

## 2.5 Initial conditions

We used 100 initially isolated, spherical GMC's, each containing  $N_p = 10^4$  particles with mass  $m_p = 30 M_\odot$ . The clouds are distributed randomly in a disk of inner radius 30 pc, outer radius 200 pc, and a Gaussian scale height of 30 pc. Each cloud has radius 4 pc, and an initial turbulent velocity field such that  $|E_{turb}/E_{pot}| = 0.5$  (i.e., they are initially in virial equilibrium). The clouds' center of mass velocities around the GC were calculated using the potential described in Section 2.3. A snapshot of the initial conditions is

shown in Figure 2. All simulations were run using an isothermal equation of state with  $T = 100$  K. This assumption of isothermal gas is somewhat crude, but may still provide an adequate physical approximation to the real thermodynamics in dense molecular gas (Wolfire et al. 1995; Pavlovski et al. 2006).

## 2.6 Convergence and consistency tests

Simulations without injected turbulence experience runaway gravitational collapse, causing the simulation to fail within  $\sim 0.1 - 0.3$  Myrs. We thus note the importance of the turbulence injection method introduced in this paper. However, turbulence injected too infrequently leads to unphysical results, so it is important to inject it relatively often.

The turbulence driving method described in Section 2.4, in practice, adds an additional velocity “kick” due to turbulence to each particle every  $N_t$  timesteps. The energy  $\Delta E_{in}$  injected per  $N_t$  timesteps is kept constant. With these two free parameters we conducted several tests to find the optimal values to use. We varied the energy input  $\Delta E_{in}$  from  $10^{46}$  to  $10^{50}$  ergs, and  $N_t$  from 1 to 5. See appendix B for more information. Our tests led us to the choice of  $N_t = 2$ ,  $\Delta E_{in} = 10^{47}$  ergs. In addition, we check whether the angular momentum of the gas is conserved when turbulence is added. As the system is nearly axisymmetric on the scale



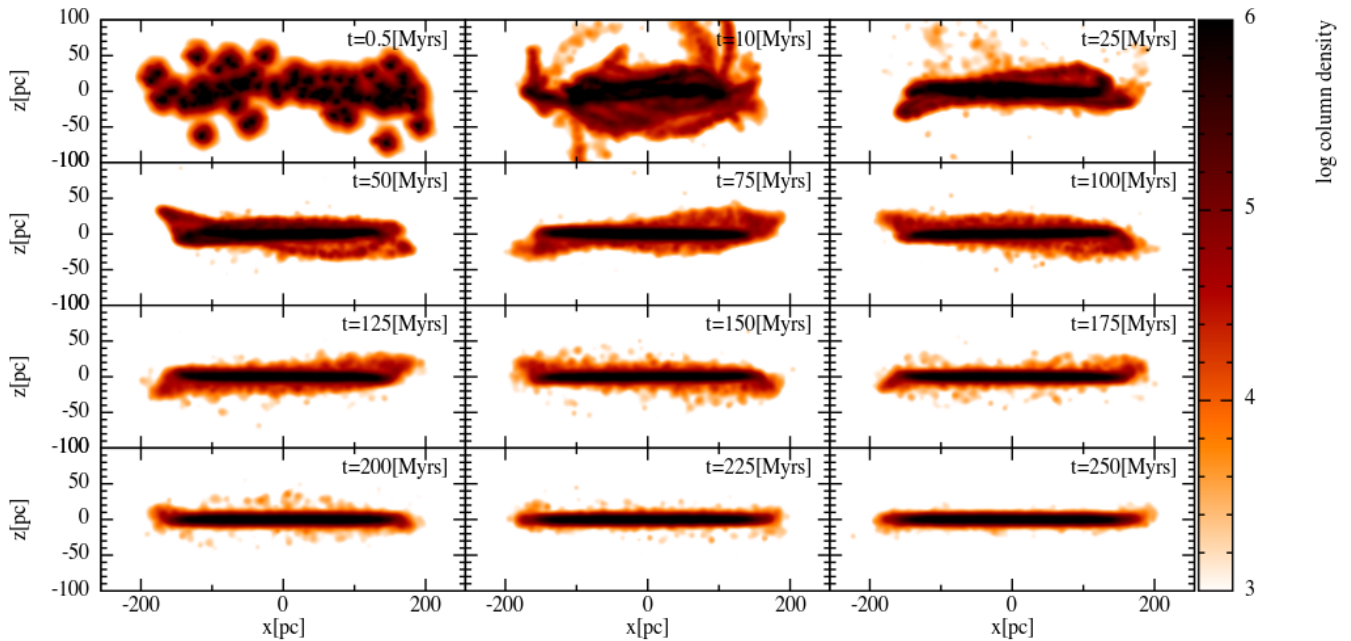


**Figure 3.** Column number density at different times, edge-on view. The long axis of the bar is oriented along the  $x$ -axis. Color map in log scale. Units are in  $\text{cm}^{-3}$  pc. The precession period of  $\sim 50$  Myrs can be seen in the back and forth tilt in the  $z$ - $x$  plane.

we consider here, angular momentum should be conserved (at least on short timescales). Indeed we find that overall angular momentum is conserved (see Figure B1).

### 3 RESULTS

We ran the system for 250 Myrs, using the turbulence parameters described in Section 2.6. The edge-on view of the resulting column density evolution of our simulation is presented in Figure 3, which can be used to compare with observations. Figure 4 shows the face-on column density evolution.

#### 3.1 Spiral structure

The initial clouds are tidally stretched relatively quickly, and the resulting streams coalesce into a disk with a flocculent spiral pattern and an inner inner cavity of radius  $\sim 30$  pc. This cavity then closes slowly over time, as gas migrates inward. After  $\sim 50$  Myrs, the gas settles into a quasi-steady state (because of the constantly injected turbulence, a perfect steady state cannot occur).

Figure 4 shows the spiral pattern continuously appearing and then partially dissipating, which is caused by our injected turbulence. A similar result was found for galactic scales, e.g., in D’Onghia et al. (2013), where they found that the spiral patterns in their simulations of self-gravitating disks of stars are not global as predicted by classical static density wave theory, but locally they appear to fluctuate in amplitude with time. Their spirals are actually segments produced by local under-dense and over-dense regions. These under-dense and over-dense regions act as perturbers, maintaining the spiral pattern. Their results can be compared to ours, although, it is the injected turbulence that acts as the local perturber in the gas.

#### 3.2 Density evolution and precession

In Figure 5 (top panel) we show the time evolution of the average number density,  $n_{ave}$ . The values shown in the figure are slightly lower than the average densities observed in the CMZ ( $n_{obs} \sim 5 \times 10^3 - 5 \times 10^4 \text{ cm}^{-3}$ , e.g., Kruijssen et al. 2015; Henshaw et al. 2016). The density evolution also exhibits oscillations with a period of  $\sim 50$  Myrs. Additionally, the gas disk precesses due to the external potential with a similar period. This behavior is depicted in Figure 5 (middle panel), where  $\phi_l$  is defined as:

$$\phi_l = \arctan \frac{l_y}{l_x}, \quad (7)$$

and  $l_x$  and  $l_y$  are the  $x$  and  $y$  components of the total angular momentum vector, respectively. We find that this precession timescale correlates with the density oscillations<sup>2</sup>. Finally, we show in the bottom panel of Figure 5 the time evolution of the angle  $\theta_l$ , i.e., the angle between the  $z$  axis and the total angular momentum vector:

$$\theta_l = \arctan \frac{l_z}{L}, \quad (8)$$

where  $l_z$  is the  $z$  component of angular momentum vector, and  $L$  is its magnitude. We note that  $\theta_l$  decreases over time, reaching an almost zero value after  $\sim 150$  Myrs. Also, for the first  $\sim 150$  Myrs of the simulation,  $\theta_l$  nutates with a period which is approximately half the precession timescale.

Furthermore, the density oscillations shown in Figure 5 could enhance episodes of star formation in the CMZ, which have been theorized by, e.g., Krumholz & Kruijssen (2015). Their study finds that the characteristic timescale for star

<sup>2</sup> We confirmed the correlation between the density oscillations and the disk precession by testing a more oblate potential than the one described in Section 2.3.

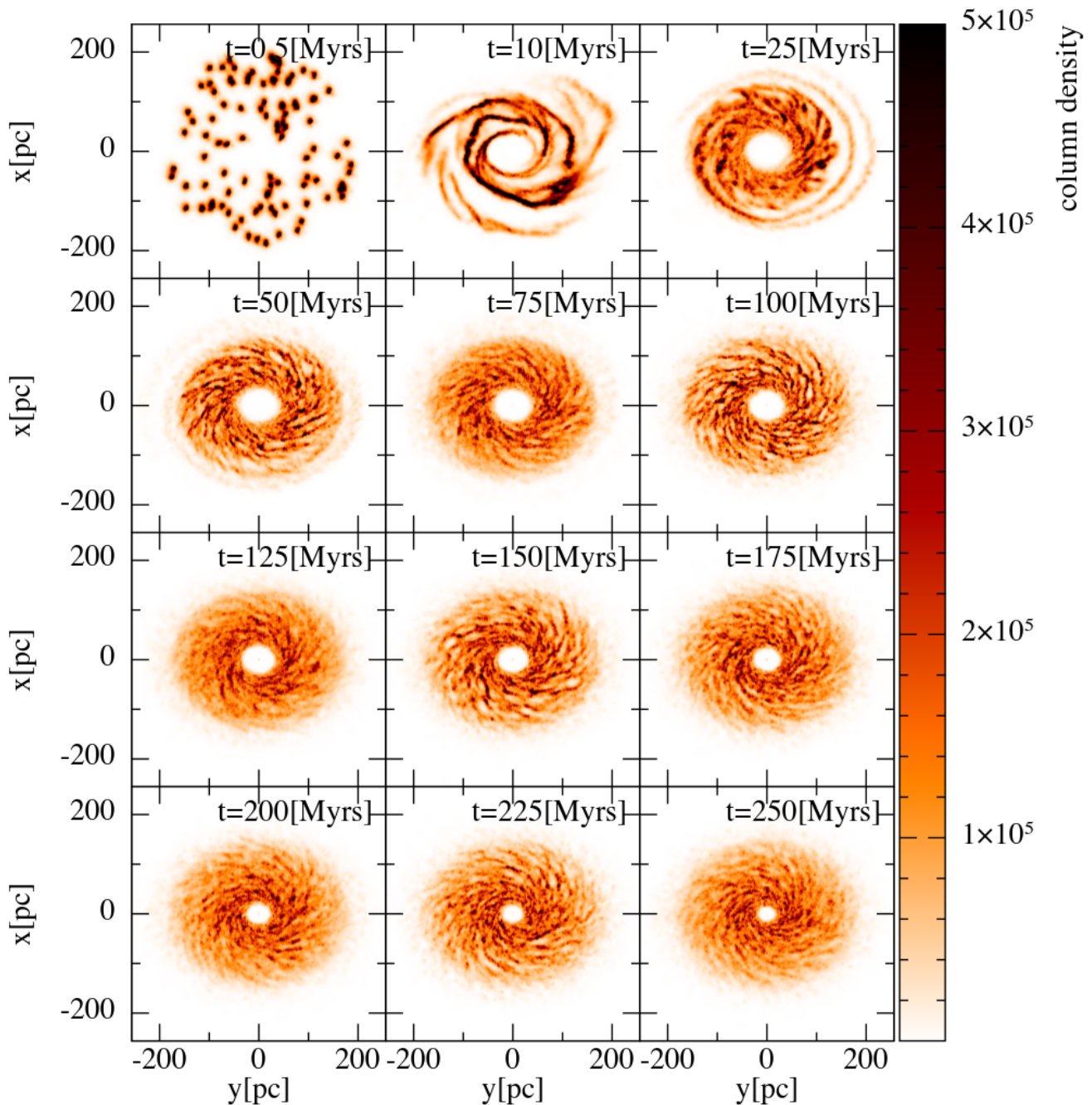


**Figure 4.** Column number density at different times, top-down view. The long axis of the bar is oriented along the x-axis. Color map in linear scale. Units are in  $\text{cm}^{-3} \text{ pc}$ . High-density regions are visible at  $t = 50, 100, 150, 200$  and  $250$  Myrs. The plots are rotated so that the vertical axis corresponds to the x-axis.

formation is of the order of 10-20 Myr, which compares favorably to the 50 Myr density oscillation timescale in our simulation.

### 3.3 Vertical structure

The steady-state dynamics of a gas in a disk/bar-like potential can be estimated analytically. For example, the scale height of a gas disk can be computed via:

$$H(r) \sim \frac{v_s}{\Omega(r)}, \quad (9)$$

where  $v_s$  is the gas' velocity dispersion and  $\Omega$  is the angular velocity due to the Galactic potential, i.e.,

$$\Omega(r) = \frac{1}{r} \sqrt{r \frac{d\Phi}{dr}}. \quad (10)$$

The potential  $\Phi$  (see Section 2.3), which dictates the dynamical evolution of the gas, deviates significantly from a Keplerian potential and is determined mostly by the stellar population. The enclosed mass at 200 pc is about  $10^9 M_\odot$  (Kim et al. 2011). The velocity dispersion in our case is dominated by the injected turbulence. After the gas has reached a

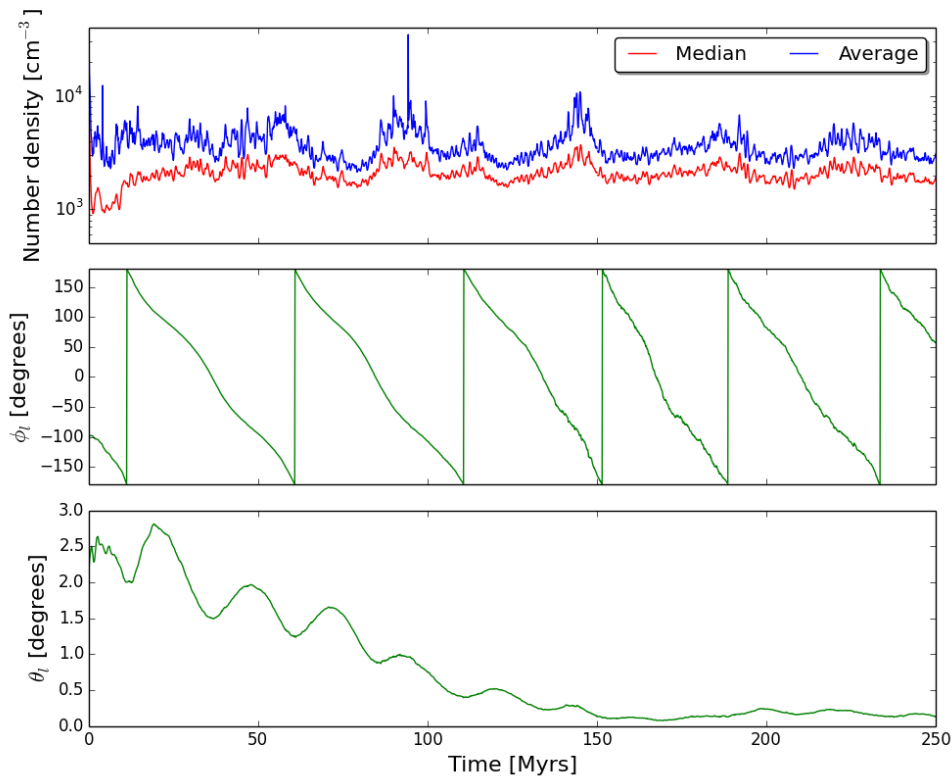


**Figure 5.** Top: time evolution of the average and median number density of the gas, computed by taking the average (and median) of all the particles’ densities. Density oscillations occur every  $\sim 50$  Myrs. Middle: time evolution of the azimuthal angle of the angular momentum vector (Equation 7). The precession timescale of the gas disk ( $\sim 50$  Myrs) correlates with the density oscillations. Bottom: time evolution of the polar angle of the total angular momentum vector,  $\theta_t$  (Equation 8). The value of  $\theta_t$  decreases over time. Also, it shows a nutation with a timescale approximately half the precession timescale.

steady-state, we find that the dispersion velocity in the simulation is about  $8 \text{ km s}^{-1}$ . Plugging this value into Equation 9 results in a scale height of about 10 pc at a radius of 100 pc from the center. In Figure 6 we show six time snapshots of the  $z$ - $r$  phase space. The red line indicates the expected disk scale height while assuming a constant velocity dispersion<sup>3</sup>.

After  $\sim 50$  Myrs, the gas reached a steady state and settled into a thin disk with a number density  $\sim 5 \times 10^3 \text{ cm}^{-3}$ . However, we also find that before a steady state is reached, the system seems consistent with current day observations (i.e., an  $\infty$ -shaped ring, see Molinari et al. 2011; Kruijssen et al. 2015; Henshaw et al. 2016). A similar result was found in Shin et al. (2017): their simulations show a twisted ring during the first 100 Myrs of their simulation.

In Figure 7 we compare between the edge-on view of our simulation at 10 Myr and observations adopted from Molinari et al. (2011), shown in black and white. This result suggests that the observed gas in the CMZ may not be currently in a dynamical steady-state. This timescale of 10 Myr is consistent with observations that suggest that the CMZ has undergone starburst and AGN activity within the past  $\sim 10$  Myrs, as revealed by the existence of the Fermi bubbles (Su et al. 2010; Zubovas et al. 2011) and three similarly-

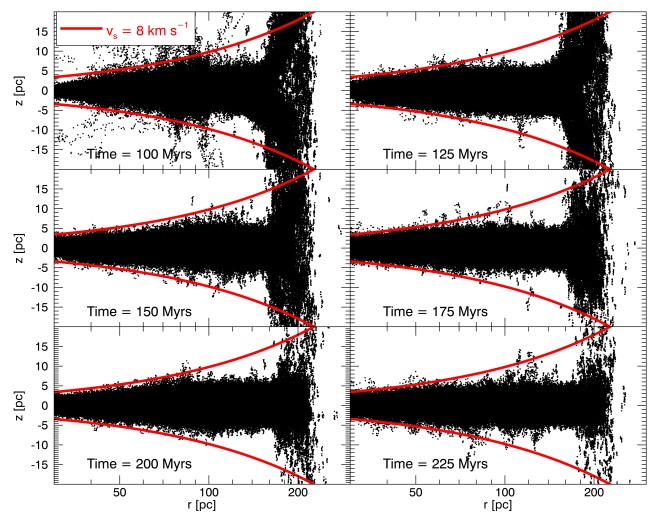


**Figure 6.** Plots of  $z$  vs  $r$  at different times. We indicate with a red line the computed scale height using Equation 9 and a velocity dispersion of  $8 \text{ km s}^{-1}$ .

aged (same order of magnitude) young massive star clusters (Clarkson et al. 2012; Hußmann et al. 2012; Lu et al. 2013).

<sup>3</sup> Note that the velocity dispersion estimated from observations of the CMZ, i.e.  $15 \text{ km s}^{-1}$ , is about a factor of two greater than the one we find in our simulation (e.g., Morris & Serabyn 1996).

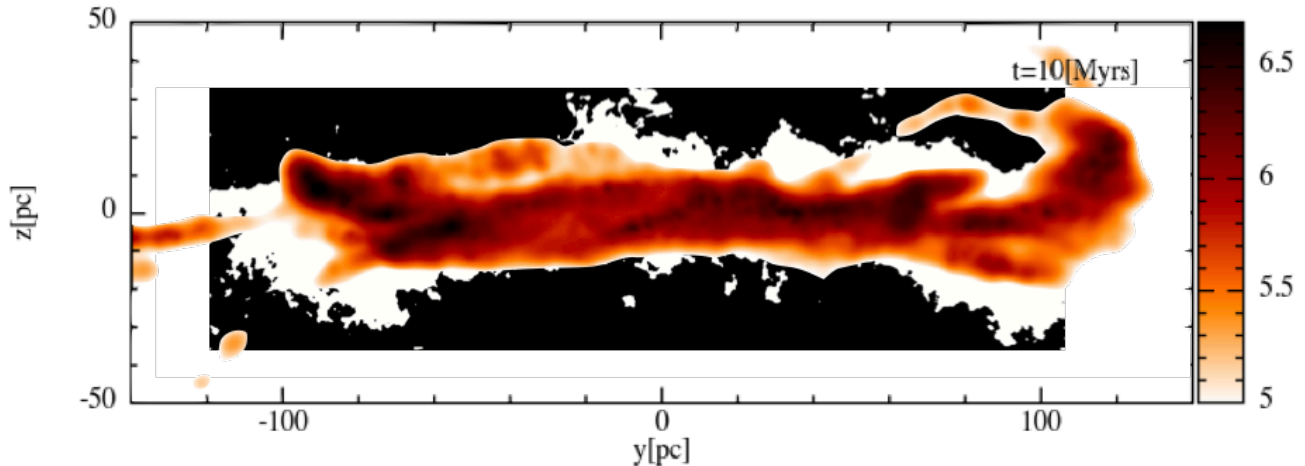


**Figure 7.** Column number density at  $t = 10$  Myrs. We remove particles with  $n < 100 \text{ cm}^{-3}$ , and adjusted the column density range to highlight the twisted ring shape. We superimposed our plot with a black and white shadow of the observed twisted ring (Figure 2 from Molinari et al. 2011) for comparison. The observed twisted ring plot has been rotated 180 degrees around the  $z$  axis for better comparison with our simulation.

#### 4 SUMMARY

Turbulence plays an important role in the dynamics of the CMZ. Thus, it is necessary to understand the dynamical evolution of turbulence-driven gas with self-gravity. In this paper we describe a simulation of the CMZ using the SPH code Gadget2, in which we include the gravitational potential of the inner 300 pc, and a recipe for turbulence driving. We demonstrated that driven turbulence is imperative to balance the gas' gravitational collapse.

Our turbulence injection recipe is modelled based on the method described by Mac Low (1999). We create spatially static turbulent velocity fields (in the form of cubic lattices), for which the amplitude is adjusted in time to maintain a constant energy input.  $64^3$  of these cubic lattices were used to fill the volume of a large simulation box, along with trilinear interpolation to calculate the velocity kicks to every gas particle.

Starting with clouds in our initial conditions, our turbulence driving method allows us to study the interaction between the self-gravity of the gas and turbulence over long timescales. Our results can be summarized as follows:

We found that the clouds are stretched quickly into tidal streams, which then form a twisted ring. This vertical structure resembles observations, but only during the first 10-20 Myrs of simulation time. This result leads us to conclude that the CMZ is likely not currently in a dynamical steady state. The vertical structure dissipates, leaving behind a smooth, flat disk after approximately 20 Myrs.

Furthermore, we also found that the gas disk precesses due to the influence of the galactic potential, with a timescale of  $\sim 50$  Myrs. This precession also correlates with density oscillations which occur on a similar timescale. These density oscillations could enhance episodes of star formation in the CMZ, which have been proposed in by previous studies (e.g., Krumholz & Kruijssen 2015).

We note that there are several physical processes (stellar feedback, magnetic fields, etc) that we are not accounting for

in this study. In addition, our simulation does not have sufficient spatial resolution to study the small-scale evolution of the gas. Nonetheless, our results show that the turbulence injection recipe introduced here is capable of balancing the self-gravity of the gas, which allows us to run the simulation for long timescales. The results of this work show that a complete description of large-scale gas dynamics in a galactic nucleus requires the inclusion of a source of turbulence driving, whether it be akin to the treatment that we have employed here, or whether the turbulence emerges naturally from a hydrodynamic or magnetohydrodynamic treatment that incorporates the important dynamical instabilities.

#### ACKNOWLEDGMENTS

All column density plots were done using the SPH visualization software SPLASH (Price 2007). J.M.S would like to thank Paul Clark for his help on adapting the external pressure term into Gadget2, and to Sofia G. Gallego and Sungsoo S. Kim for their help implementing the gravitational potential of the inner Galaxy. This material is based upon work supported by the National Science Foundation Graduate Research Fellowship Program under Grant No. DGE-1144087. This work used computational and storage services associated with the Hoffman2 Shared Cluster provided by UCLA Institute for Digital Research and Education's Research Technology Group. This work also used the Extreme Science and Engineering Discovery Environment (XSEDE) Comet at the San Diego Supercomputer Center at UC San Diego through allocations AST170039 and AST180051. XSEDE is supported by National Science Foundation grant number ACI-1548562.



## APPENDIX A: CONSTANT ENERGY INPUT RATE

In this appendix we derive equation 6.

Our algorithm adds a velocity “kick” to each particle every  $N_t$  timesteps while maintaining a constant energy input rate  $\dot{E}_{in} = \Delta E_{in}/(N_t \Delta t)$ , where  $\Delta t$  is the simulation timestep (fixed to be equal to 1000 yrs), and:

$$\Delta E_{in} = E_2 - E_1 = \frac{1}{2} m_p \sum_{i=1}^{N_{sph}} \vec{v}_{2,i} \cdot \vec{v}_{2,i} - \frac{1}{2} m_p \sum_{i=1}^{N_{sph}} \vec{v}_{1,i} \cdot \vec{v}_{1,i}, \quad (\text{A1})$$

where  $\vec{v}_{1,i}$  is the velocity vector of a particle at time  $t_1$  (before the kick), and

$$\vec{v}_{2,i} = \vec{v}_{1,i} + A \Delta \vec{v}_i = \vec{v}_{1,i} + A \sqrt{G \rho_i} \vec{I}_i(x, y, z) \quad (\text{A2})$$

is the velocity of the particle at time  $t_2$  (after the kick). Therefore,  $t_2 - t_1 = N_t \Delta t_s$ . The function  $\vec{I}(x, y, z)$  is the interpolation function that represents the turbulent velocity increment based on the particle’s position (hereafter called  $\vec{I}$ ), and  $A$  is the target variable.

Equation A1 then becomes:

$$\Delta E_{in} = \frac{1}{2} m_p \left[ \sum_{i=1}^{N_{sph}} \left( \vec{v}_{1,i} + A \sqrt{G \rho_i} \vec{I}_i \right) \cdot \left( \vec{v}_{1,i} + A \sqrt{G \rho_i} \vec{I}_i \right) - \sum_{i=1}^N \vec{v}_{1,i} \cdot \vec{v}_{1,i} \right] \quad (\text{A3})$$

By simplifying Equation A3, the result is:

$$\Delta E_{in} = \frac{1}{2} m_p \sum_{i=1}^{N_{sph}} \left[ A^2 G \rho_i \vec{I}_i \cdot \vec{I}_i + 2A \sqrt{G \rho_i} \vec{I}_i \cdot \vec{v}_{1,i} \right] \quad (\text{A4})$$

This equation always gives both positive and negative values for  $A$  and our code always chooses the positive value. However, to ensure that the injection of turbulence does not violate the conservation of total angular momentum of the gas, we simply multiply  $A$  by a factor of  $-1$  or  $+1$ , alternating between these two factors every time the driving is performed. This ensures that, over time, the net angular momentum added to the gas particles is approximately zero while keeping the same increase in energy  $\Delta E_{in}$ .

Furthermore, we change each of the  $64^3$  cubes of turbulence every time the driving is performed. This is to mimic the random nature of turbulence. Regardless of the source of turbulence, we expect that a parcel of gas will experience a coherent turbulent driving force during a given timescale. We can justify changing each grid every  $N_t$  timesteps if we consider that the crossing time of a parcel of gas traveling at an orbital speed of  $v \approx 150 \text{ km s}^{-1}$  through the average scale of a turbulence cube, i.e.,  $L_{ave} \approx 1 \text{ pc}$ , is  $t_{cross} \approx 6000 \text{ yrs}$ . Hence, as a crude approximation, there is no need for the velocity field to be coherent on timescales longer than a couple of timesteps, and thus we can replace each turbulence cube.

## APPENDIX B: DEPENDENCE ON TURBULENCE PARAMETERS

Here we describe the tests we carried out to study the performance of our turbulence algorithm in order to choose  $N_t$  and  $\Delta E_{in}$  values for our final production run. While these parameters are better represented in form of a rate, the results of this section indicate that the time interval at which

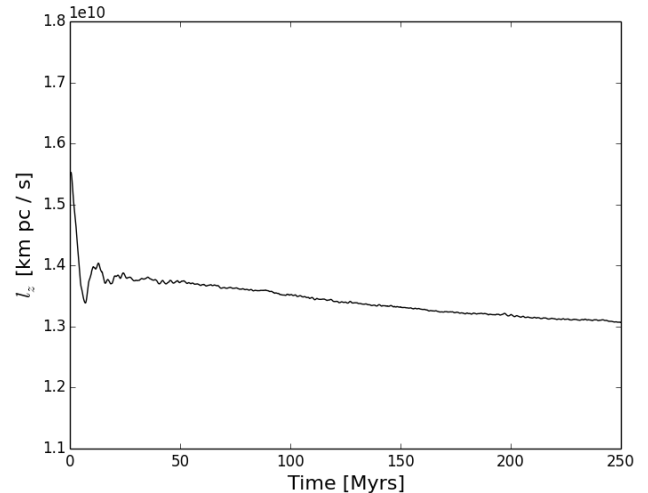


**Figure B1.** Total angular momentum decreases slightly over 250 Myrs. However, this change is so small that the angular momentum can be considered constant.

the turbulence is injected affects the subsequent evolution of the gas.

We tested driving the turbulence every 1 to 5 timesteps for a total of 25 tests: for each  $N_t$ , we used  $\Delta E_{in} = 10^{46}$  to  $10^{50}$  ergs, in a factor of 10 increments. We ran each simulation for 100 Myrs to allow the system to reach a quasi-steady state.

As proxy for the evolution of the systems, we plot the average number density ( $n_{ave}$ ) as a function of time, as shown in Figures B2 to B6. For the simulations with  $N_t = 2$  and 3, the time evolution of  $n_{ave}$  is very similar (except for the case with  $\Delta E_{in} = 10^{50}$  ergs, whose  $n_{ave}$  evolution diverges from all other runs). The average density continues oscillating, potentially reaching a steady-state by  $\sim 50$  Myrs. However, it is this time when density oscillations start to manifest.

We also plot in Figures B2 to B6 the RMS number density ( $n_{RMS}$ ) from  $t = 50 - 100$  Myrs, in order to better discern differences between runs. The runs with parameter  $N_t = 4$  and 5 show higher average densities, as expected, because in these cases gravity has more time to compress the gas to higher densities. However, given their high density RMS peaks, these runs are less consistent and more chaotic than those with lower values of  $N_t$ . Also, the runs with  $N_t = 5$  were only run for 50 Myrs due to the fact that the tests with  $\Delta E_{in} = 10^{46}$  to  $10^{48}$  ergs exhibited high density clumps which slowed down the computation time. These clumps originate because here, the turbulence is not injected often enough to support the gas against gravitational collapse. Particles pile on top of each other, and due to the nature of the kernel used by Gadget2, once the distance between particles approaches the smoothing length, the pressure gradient is no longer correct and the particles stick together, creating very high density clumps. Additionally, in Figures B2 to B6, we plot the distribution of mass fraction as a function of density (density PDF) at  $t = 50$  and 100 Myrs for each run. Inside a molecular cloud, the density PDF is shaped by the complex interaction between turbulence, self-gravity, magnetic fields and stellar feedback. As a result, it is an effective tool to determine the dynamical state of the gas (e.g. Federrath et al. 2010). In most of our test runs, the calculated den-

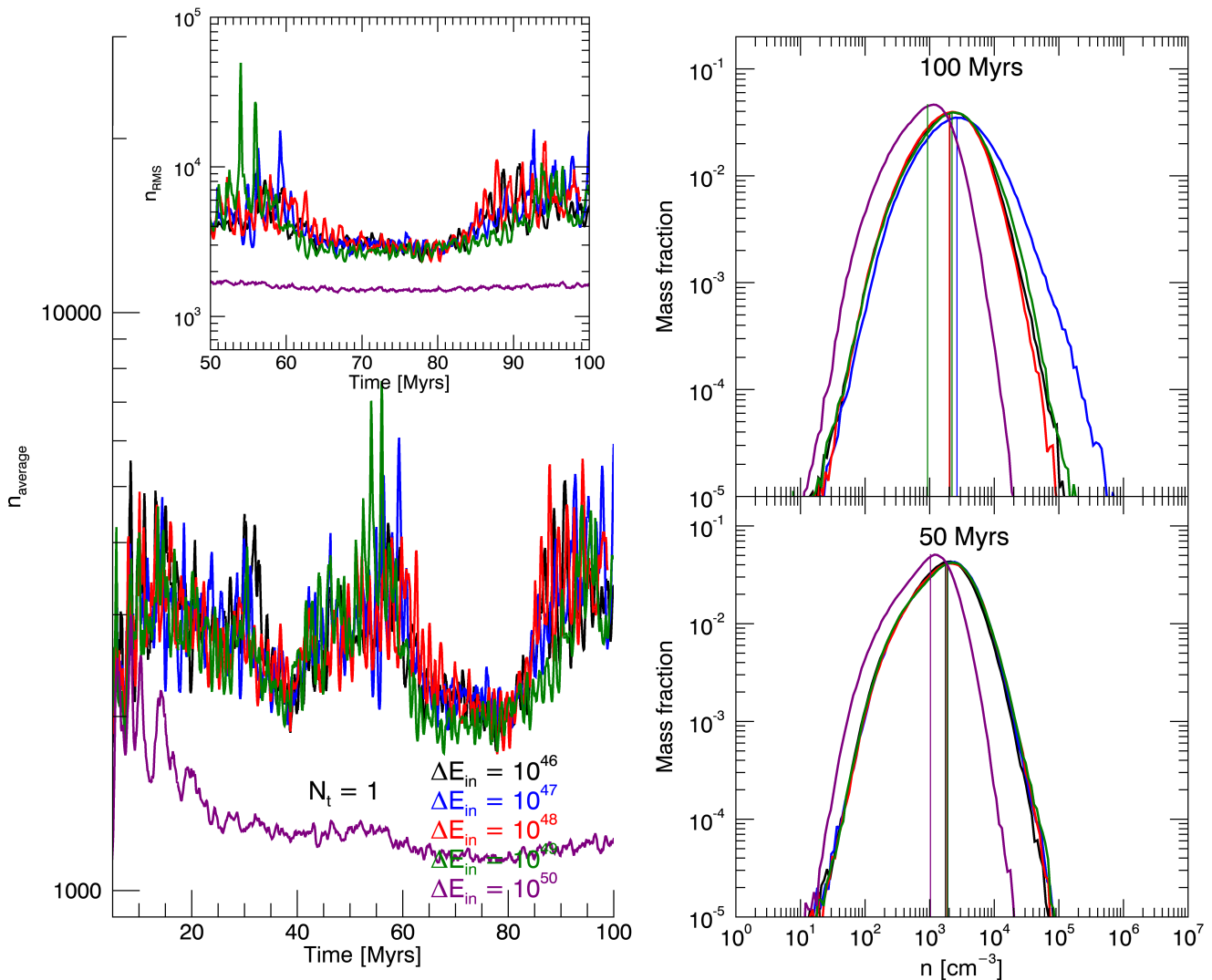


**Figure B2.** Median density, RMS density and density PDF for tests with  $N_t = 1$ . The mass-weighted median density is plotted with a vertical line. The density PDF is approximately lognormal.

sity PDF resembles a lognormal distribution, a result that several groups have found for isothermal gas (e.g., [Vazquez-Semadeni 1994](#); [Nordlund & Padoan 1999](#); [Klessen 2000](#) and others). Thus, we can fit the PDFs to Gaussian functions of  $x = \ln(n/n_0)$  with mean  $\mu$  and dispersion  $\sigma$ :

$$f_M = C \exp\left[-\frac{(x - \mu)^2}{\sigma^2}\right]. \quad (\text{B1})$$

The mass-weighted median number density (half of the mass is at densities above and below this value) is proportional to  $\exp(\mu)$ . We indicate this parameter with vertical bars in both figures.

The tests with parameter  $N_t = 2$  and 3 show better consistency in the range of densities observed in the GC ( $n \sim 10^{3-4} \text{ cm}^{-3}$ ) than the other test runs. The exact choice of parameters will have little effect on our results, thus we opted for the  $N_t = 2$  and  $\Delta E_{in} = 10^{47}$  ergs for our final production run.

As a final check, we confirmed that the simulation with the chosen values for  $N_t$  and  $\Delta E_{in}$  conserve angular momentum over long timescales. Figure [B1](#) shows that angular mo-

mentum slightly decreases, from  $\sim 1.4 \times 10^{10} \text{ km s}^{-1} \text{ pc}$  at 50 Myrs to  $1.3 \times 10^{10} \text{ km s}^{-1} \text{ pc}$  at 250 Myrs, a difference of  $\sim 1\%$ . This change is so small that we can consider the angular momentum constant for the timescale we consider here.

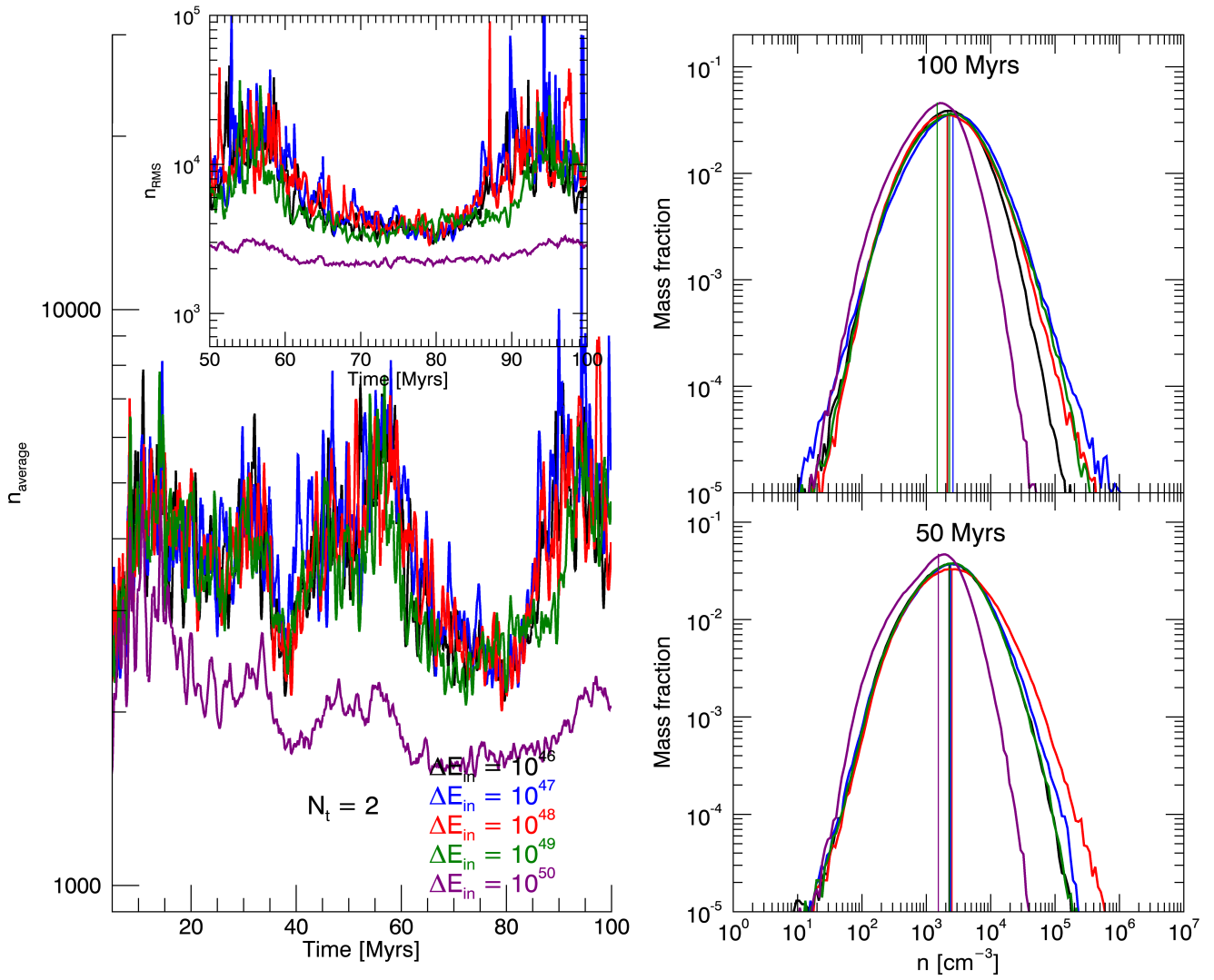


**Figure B3.** Median density, RMS density and density distribution function for tests with  $N_t = 2$ . The distribution is lognormal. The mass-weighted median density is plotted with a vertical line.

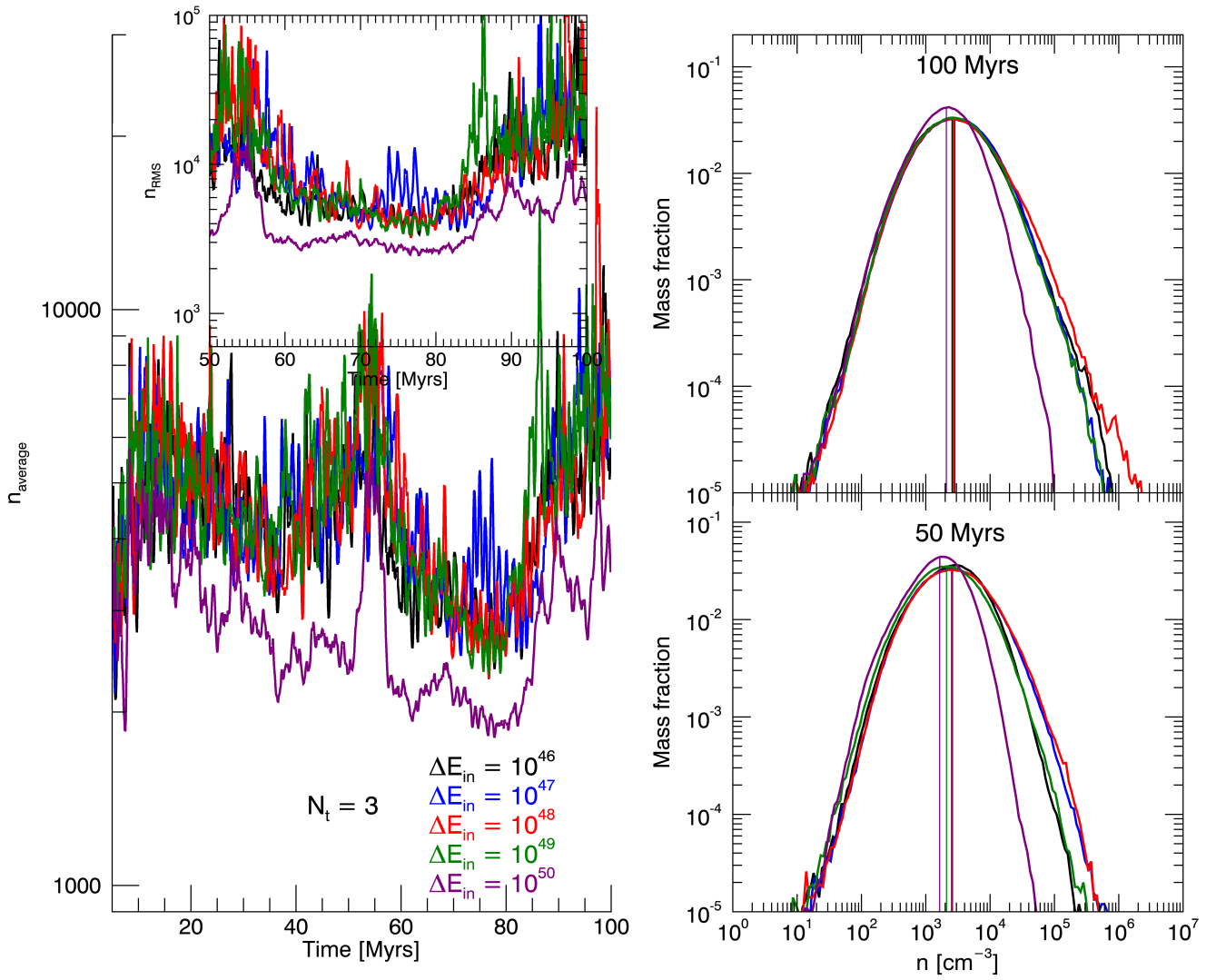


**Figure B4.** Median density, RMS density and density distribution function for tests with  $N_t = 3$ . The distribution is lognormal. The mass-weighted median density is plotted with a vertical line.



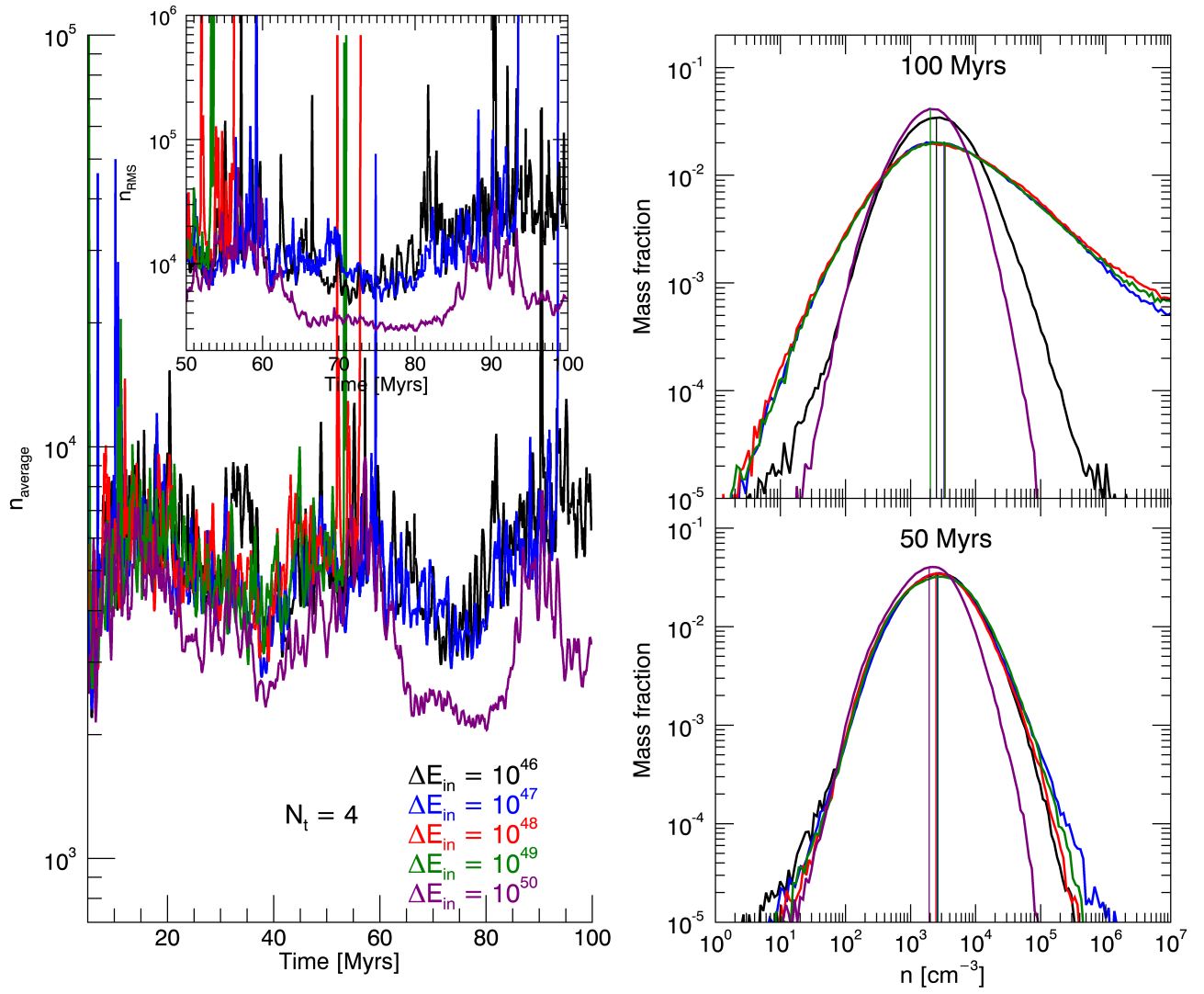


**Figure B5.** Median density, RMS density and density distribution function for tests with  $N_t = 4$ . The distribution is lognormal. The mass-weighted median density is plotted with a vertical line.

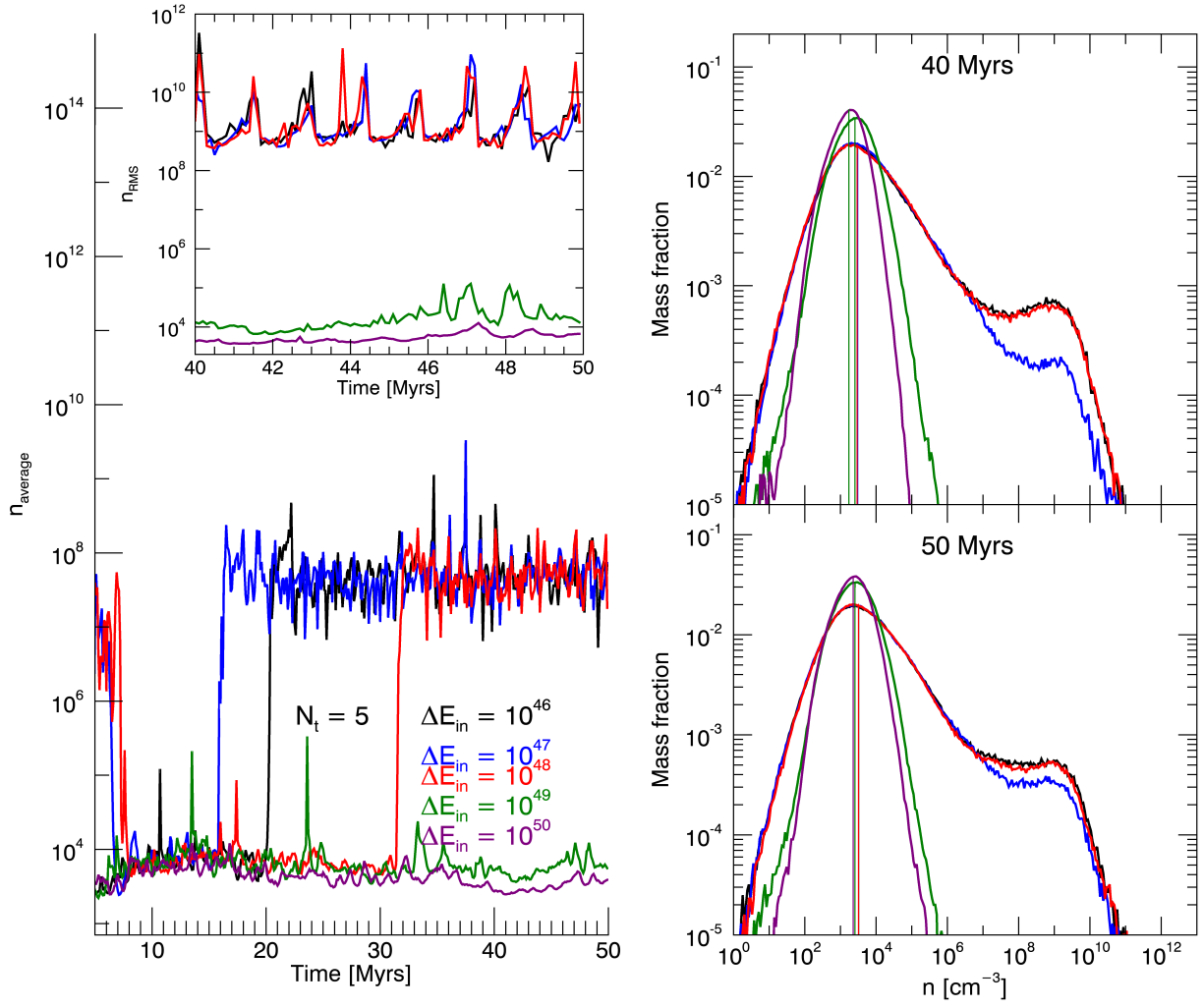


**Figure B6.** Median density, RMS density and density distribution function for tests with  $N_t = 5$ . The mass-weighted median density is plotted with a vertical line. These tests were run only up to 50 Myrs. The density PDF of the runs with  $\Delta E_{in} = 10^{46} - 10^{48}$  ergs deviate dramatically from lognormal.

**REFERENCES**

Ao Y., et al., 2013, *A&A*, **550**, A135  
 Athanassoula E., 1992, *MNRAS*, **259**, 345  
 Balsara D. S., 1995, *Journal of Computational Physics*, **121**, 357  
 Binney J., Gerhard O. E., Stark A. A., Bally J., Uchida K. I., 1991, *MNRAS*, **252**, 210  
 Bland-Hawthorn J., Gerhard O., 2016, *ARA&A*, **54**, 529  
 Burkhardt B., Falceta-Gonçalves D., Kowal G., Lazarian A., 2009, *ApJ*, **693**, 250  
 Clark P. C., Glover S. C. O., Klessen R. S., Bromm V., 2011, *ApJ*, **727**, 110  
 Clarkson W. I., Ghez A. M., Morris M. R., Lu J. R., Stolte A., McCrady N., Do T., Yelda S., 2012, *ApJ*, **751**, 132  
 D’Onghia E., Vogelsberger M., Hernquist L., 2013, *ApJ*, **766**, 34  
 Federrath C., Roman-Duval J., Klessen R. S., Schmidt W., Mac Low M.-M., 2010, *A&A*, **512**, A81  
 Gallego S. G., Cuadra J., 2017, *MNRAS*, **467**, L41  
 Gerhard O. E., 1996, in Blitz L., Teuben P. J., eds, *IAU Symposium Vol. 169, Unsolved Problems of the Milky Way*. p. 79 ([arXiv:astro-ph/9604069](https://arxiv.org/abs/astro-ph/9604069))  
 Ginsburg A., et al., 2016, *A&A*, **586**, A50  
 Güsten R., Walmsley C. M., Pauls T., 1981, *A&A*, **103**, 197  
 Henshaw J. D., et al., 2016, *MNRAS*, **457**, 2675  
 Huettemeister S., Wilson T. L., Bania T. M., Martin-Pintado J., 1993, *A&A*, **280**, 255  
 Hußmann B., Stolte A., Brandner W., Gennaro M., Liermann A., 2012, *A&A*, **540**, A57  
 Immer K., Kauffmann J., Pillai T., Ginsburg A., Menten K. M., 2016, *A&A*, **595**, A94  
 Jenkins A., Binney J., 1994, *MNRAS*, **270**, 703  
 Khoperskov S. A., Vasiliev E. O., Sobolev A. M., Khoperskov A. V., 2013, *MNRAS*, **428**, 2311  
 Kim S. S., Saitoh T. R., Jeon M., Figer D. F., Merritt D., Wada K., 2011, *ApJ*, **735**, L11  
 Klessen R. S., 2000, *ApJ*, **535**, 869  
 Kruijssen J. M. D., Longmore S. N., Elmegreen B. G., Murray N., Bally J., Testi L., Kennicutt R. C., 2014, *MNRAS*, **440**, 3370  
 Kruijssen J. M. D., Dale J. E., Longmore S. N., 2015, *MNRAS*, **447**, 1059  
 Krumholz M. R., Kruijssen J. M. D., 2015, *MNRAS*, **453**, 739  
 Krumholz M. R., McKee C. F., 2005, *ApJ*, **630**, 250  
 Lu J. R., Do T., Ghez A. M., Morris M. R., Yelda S., Matthews K., 2013, *ApJ*, **764**, 155  
 Lucas W. E., 2015, PhD thesis, University of St Andrews  
 Mac Low M.-M., 1999, *ApJ*, **524**, 169  
 Mac Low M.-M., Klessen R. S., Burkert A., Smith M. D., 1998, *Physical Review Letters*, **80**, 2754  
 Molinari S., et al., 2011, *ApJ*, **735**, L33  
 Monaghan J. J., Gingold R. A., 1983, *Journal of Computational Physics*, **52**, 374  
 Morris M., Serabyn E., 1996, *ARA&A*, **34**, 645  
 Morris M., Polish N., Zuckerman B., Kaifu N., 1983, *AJ*, **88**, 1228  
 Namekata D., Habe A., 2011, *ApJ*, **731**, 57  
 Nordlund Å. K., Padoan P., 1999, in Franco J., Carraminana A., eds, *Interstellar Turbulence*. p. 218 ([arXiv:astro-ph/9810074](https://arxiv.org/abs/astro-ph/9810074))  
 Padoan P., Jimenez R., Nordlund Å., Boldyrev S., 2004, *Physical Review Letters*, **92**, 191102  
 Pavlovski G., Smith M. D., Mac Low M.-M., 2006, *MNRAS*, **368**, 943  
 Portail M., Gerhard O., Wegg C., Ness M., 2017, *MNRAS*, **465**, 1621  
 Price D. J., 2007, *Publ. Astron. Soc. Australia*, **24**, 159  
 Ridley M. G. L., Sormani M. C., Treß R. G., Magorrian J., Klessen R. S., 2017, *MNRAS*, **469**, 2251  
 Rogallo R. S., 1981, *NASTM*, 81315  
 Schmidt W., Hillebrandt W., C. Niemeyer J., 2006, **35**, 353  
 Shin J., Kim S. S., Baba J., Saitoh T. R., Hwang J.-S., Chun K., Hozumi S., 2017, *ApJ*, **841**, 74  
 Sormani M. C., Binney J., Magorrian J., 2015a, *MNRAS*, **449**, 2421  
 Sormani M. C., Binney J., Magorrian J., 2015b, *MNRAS*, **451**, 3437  
 Sormani M. C., Treß R. G., Ridley M., Glover S. C. O., Klessen R. S., Binney J., Magorrian J., Smith R., 2018, *MNRAS*, **475**, 2383  
 Spergel D. N., Blitz L., 1992, *Nature*, **357**, 665  
 Springel V., 2005, *MNRAS*, **364**, 1105  
 Springel V., Hernquist L., 2002, *MNRAS*, **333**, 649  
 Stone J. M., Ostriker E. C., Gammie C. F., 1998, *ApJ*, **508**, L99  
 Su M., Slatyer T. R., Finkbeiner D. P., 2010, *ApJ*, **724**, 1044  
 Vazquez-Semadeni E., 1994, *ApJ*, **423**, 681  
 Wada K., 2001, *ApJ*, **559**, L41  
 Wolfire M. G., Hollenbach D., McKee C. F., Tielens A. G. G. M., Bakes E. L. O., 1995, *ApJ*, **443**, 152  
 Zhao H., Spergel D. N., Rich R. M., 1994, *AJ*, **108**, 2154  
 Zubovas K., King A. R., Nayakshin S., 2011, *MNRAS*, **415**, L21

This paper has been typeset from a  $\text{\TeX}/\text{\LaTeX}$  file prepared by the author.